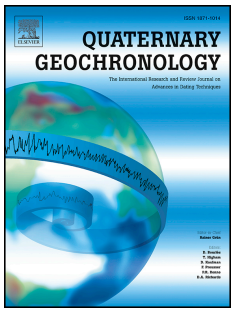

Electron spin resonance dating of quartz from archaeological sites at Victoria Falls, Zambia

Marcus Richter, Sumiko Tsukamoto, Melissa S. Chapot, Geoff A.T. Duller, Lawrence S. Barham

PII: S1871-1014(22)00093-0

DOI: https://doi.org/10.1016/j.quageo.2022.101345

Reference: QUAGEO 101345

To appear in: *Quaternary Geochronology*

Received Date: 1 December 2021

Revised Date: 30 April 2022

Accepted Date: 16 May 2022

Please cite this article as: Richter, M., Tsukamoto, S., Chapot, M.S., Duller, G.A.T., Barham, L.S., Electron spin resonance dating of quartz from archaeological sites at Victoria Falls, Zambia, *Quaternary Geochronology* (2022), doi: https://doi.org/10.1016/j.quageo.2022.101345.

Electron spin resonance dating of quartz from archaeological sites at Victoria Falls, Zambia

Marcus Richter[a*], Sumiko Tsukamoto[a], Melissa S. Chapot[b], Geoff A.T. Duller[b], Lawrence S. Barham[c]

[a]Department of Geochronology, Leibniz Institute for Applied Geophysics (LIAG), Stilleweg 2, Hannover, 30655, Germany

[b]Department of Geography and Earth Sciences, Aberystwyth University, Aberystwyth, SY23 3DB, UK

[c]Department of Archaeology, Classics and Egyptology, University of Liverpool, Liverpool, L69 7WZ, UK

*Corresponding author; Email: richter_marcus@gmx.de

Abstract

When electron spin resonance (ESR) is applied to sedimentary quartz, dealing with the poor bleachability of the signals is particularly challenging. In this study, we used both the single-grain optically stimulated luminescence (OSL) and the single aliquot ESR dating of quartz from deep sand deposits preserving a Stone Age archaeological sequence to combine the advantages of the two methods: good bleaching behaviour and extended age range. Using the youngest samples at each sampling site we were able to calculate the mean ESR residual age from the difference between the OSL ages and the apparent ESR ages. Focusing mainly on the single aliquot regenerative dose (SAR) protocol here, we were able to calculate the mean ESR residual age for the Ti and Al centres, including the non-bleachable signal component for the latter. For the NP site, residual ages of 209 ± 13 ka and 695 ± 23 ka were calculated for the two centres, whereas for the ZS site 268 ± 39 ka and 742 ± 118 ka were determined. These residual ages are significant and cannot be neglected. Thus, the residual age was subtracted from the apparent ESR ages. The validity of the residual subtraction method was tested through a

comparison of the oldest OSL age from each site with the residual subtracted ESR age. For both NP and ZS sites, the residual subtracted Ti and Al ages were consistent with the OSL age within 2-σ uncertainty, and therefore confirm the robustness of the subtraction method. Within the NP sequence, we were able to locate the end of the Early Stone Age at 590 ± 86 ka, and this provides a maximum age for the transition to the Middle Stone Age in this part of south-central Africa.

Key words: Quartz, ESR dating, Victoria Falls

1. Introduction

The Early to Middle Stone Age transition in Africa marks a change in technology with the long-lived Acheulean traditions of large cutting tools replaced by small Middle Stone Age flake and blade tools linked to the innovation of hafting with its adaptive advantage of increased efficiency of tools with handles (Coe et al., 2022). The beginning of the transition in Africa, dated by $^{40}Ar/^{39}Ar$, U-series, electron spin resonance (ESR) of tooth enamels and luminescence techniques, ranges from ~500 ka to 300 ka in southern Africa and eastern Africa. Although the identification of hafting traces is disputed, Middle Stone Age technologies are evident in these regions and in north Africa by 300 ka (Tryon et al., 2006; Wilkins et al., 2012 cf. Rots and Plisson, 2014; Sahle et al., 2013 cf. Douze et al., 2018; Hublin et al., 2017; Deino et al., 2018).

By comparison, the start of the transition in south-central Africa is poorly known with only a single locality currently dated (Kalambo Falls, Zambia), using thermally transferred optically stimulated luminescence (TT-OSL) and with large uncertainties (Duller et al., 2015). They dated fluvial sediments containing numerous stone tools from the riverbanks of the Kalambo Falls, Zambia, TT-OSL. By using this luminescence dating method, they were able to extend the age beyond the range of conventional quartz OSL dating and allowed them to place the Mode 2/3 transition between 500 and 300 ka. Unfortunately, the ages obtained from sediments containing Mode 2 stone tools showed a large scatter, which resulted in the wide range for the transition. For the upper part of the fluvial sediment sequence, they observed much larger TT-OSL equivalent doses (D_e) than those of OSL. Thus, the mean residual dose for the TT-OSL obtained from the difference between the TT-OSL and OSL D_e (~110 Gy), was subtracted from the apparent TT-OSL D_e for age calculation for older samples whose natural OSL signal was in saturation.

An aim of the 'Deep Roots Project' (2017-2022) has been to extend and refine the chronology of the Early to Middle Stone Age transition in this region, which forms a

geographical link between eastern and southern Africa. The area of Zambia in the vicinity of Victoria Falls (Mosi oa Tunya National Park) is the focus this paper as it provides up to ~34 m deep deposit of aeolian sands that preserve Early and Middle Stone Age artefact clusters. We report here on the methods and results of quartz ESR dating from a section through the sands (the NP and ZS sequences) with Early Stone Age (Acheulean) artefacts at its base, and from separate individual sites. The results provide a foundation for dating the Early to Middle Stone Age transition in this area of south-central Africa.

In trapped charge dating, it is important to estimate the degree of signal depletion achieved during transport at the time the sediment is buried. ESR signals from quartz used for dating are known be difficult to bleach; for instance the Al centre requires around 1000 h of bleaching under artificial light exposure to drop to an unbleachable signal level, while the Ti centre can be fully bleached within several tens to hundreds of hours (e.g. Toyoda et al., 2000). A number of ESR Al and Ti centre residual doses and ages for young or modern analogue sediments have been reported so far (e.g. Voinchet et al., 2015; Tsukamoto et al., 2017; 2018, Timar-Gabor et al., 2020, Richter and Tsukamoto, 2022) revealing the importance of testing samples for residuals due to incomplete resetting.

Comparable to the work of Duller et al. (2015), in this study we introduce a similar approach, combining the quartz OSL and ESR dating to date aeolian sediment sequences containing stone artefacts near the Victoria Falls, Zambia (Fig. 1A). We compare OSL and ESR ages from young sediments (up to ~160 ka, Chapot et al., this issue) to obtain a mean ESR residual age for each of the sequences. This age is subsequently subtracted from the apparent ESR ages to calculate ages for the older samples.

2. Materials and methods

2.1 Study area and sampling

The sands sampled for this study are deposited unconformably on Batoka Basalts of the Karoo Large Igneous Province that form the Mesozoic bedrock in this part of the Zambezi Valley (Jones et al., 2001). The sands have an aeolian origin, derived from Kalahari Basin sediments to the west-southwest and include a component of local weathered basalts from the Zambezi floodplain (Garzanti et al., 2022). The episodic extension of Kalahari sands into the Zambezi Valley during the Late Pleistocene is well documented and is indicative of greater aridity or increased wind speeds compared with the present (Thomas and Burrough, 2016;

Burrough et al., 2019). The sand deposits in the Mosi oa Tunya Park, however, are homogenous in terms of grain size, lacking the structure seen in local dune systems (Thomas and Burrough, 2016). There are no identifiable palaeosols or other evidence of periodic deposition that can be traced across the exposure. Weathering and bioturbation appear to have created a massive undifferentiated sand deposit.

Our study sites are located on the east side of the Upper Zambezi River, within the Mosi oa Tunya park (Fig. 1B and C), where the thick sand deposits were exposed in a scarp. The sediments are very homogeneous, massive, well-sorted medium to coarse sand. Samples were collected at two localities (NP and ZS) separated from each other by a distance of ~ 1 km (Fig. 1C).

Within this sand the archaeological record occurs as surface clusters exposed by erosion with minimal depth of deposit (5-7 cm), and as individual surface finds. The presence of refitting flakes in the clusters (to be reported separately) indicates some element of contemporaneity within these aggregates. A coarse but coherent archaeological sequence exists in the deposit with Early Stone Age artefacts in the lower part of the sands (NP18-03), the transition from the Early to Middle Stone Age (ZS17-07, ZS18-02, ZS18-03) and Later Stone Age near the top of the sands (NP18-08, NP18-09). The content of these sites will be reported separately.

For all samples, two opaque plastic tubes were hammered into the sediment; one tube for OSL dating and the other for ESR dating purposes (cf. Fig. A1). The recovered tubes were sealed to ensure that they were light tight and stored in black plastic bags. NP18 samples (n = 9) were taken along a gully cutting through the sand scarp. ZS18 samples (n = 3) were taken circa 1 km north of the NP site in exposures adjacent archaeological clusters. In 2017, the ZS17 samples (n = 8) were collected from associated archaeological clusters and to sample the sand sequence in the central part of the sand scarp. The relative height/depth from sample to sample was measured using both a handheld GPS device and a Leica total station where available.

2.2 Sample preparation

The preparation of samples for ESR dating was conducted at the Leibniz Institute for Applied Geophysics (LIAG) in Hanover, under subdued red light. First, the samples were dry sieved with a target fraction of 150-200 microns diameter. Then 10 % HCl and 30 % H_2O_2 were applied to remove carbonates and organic matter, respectively. A heavy liquid, sodium

polytungstate, was used to separate the mixture of minerals. In order to separate the quartz rich fraction a density span between 2.62 g/cm^3 and 2.70 g/cm^3 was used. By treating the resulting samples with 40 % HF for an hour, the alpha effected outer rim of the quartz grains is removed. After etching, the samples were treated with 20 % HCl to remove precipitates before finally being rinsed. Part of the sample preparation of the ZS17 samples was carried out in the luminescence laboratory of Aberystwyth University. The chemical treatment included 10 % HCl for 2-3 weeks and 20 % H_2O_2 for 8-10 weeks. There the samples have been sieved with a target fraction of 125-150 microns and 150-180 microns. Later at LIAG, the density separation and HF etching was carried out in the same way as for the other samples.

2.3 Dose rate measurements

At the NP site in-situ measurements with a portable gamma spectrometer, consisting of an Ametek DigiDart with a 5 cm diameter NaI detector were carried out. Beside the in-situ measurements, additional samples were taken from the probing holes for laboratory gamma spectroscopy and alpha and beta counting. The latter two were done at Aberystwyth University. For further details on the alpha and beta counting and field gamma spectrometry see Chapot et al. (this issue). Laboratory gamma spectroscopy was carried out at the LIAG, Hannover, using an Ortetc N-type HPGe gamma spectrometer and 50 g or 700 g of material, depending on availability.

The dose rate calculations have used the conversion factors from Liritzis et al. (2013), beta absorption factors from Guérin et al. (2012), etching factors for beta absorption from Brennan (2003), the absorbed dose fraction of Rb from Readhead (2002) and cosmic ray calculations from Prescott and Hutton (1994). We assumed that the valley was once filled with sediment, which is subsequently eroded and therefore we use half the current depth (± 50 % error) below palaeo surface values. Water content is assumed low (5 ± 2 %). To calculate the total gamma dose rate we used the mean of the field and HPGe gamma dose rates for the NP18 samples, whereas for ZS samples only HPGe gamma data was taken.

2.4 ESR measurements and X-ray irradiations

All ESR measurements were performed on a Bruker Elexsys-II E500 X-band ESR spectrometer using a variable temperature control. By the evaporation of liquid nitrogen, the temperature inside the ER4119HS cavity was kept at 100 K. The sample size was 60 mg using

quartz glass tubes. Grain sizes were 150-200 microns for the NP18 and ZS18 samples whereas for ZS17 samples the fraction of 100-150 microns was used, due to availability. For comparison the OSL grain size used was 180-212 microns (Chapot et al., this issue). For the detection of the Al centre $[AlO_4]^0$, the following measurement settings were used: 335 ± 15 mT scanned magnetic field, modulation amplitude 0.1 mT, modulation frequency 100 kHz, 40 ms conversion time and 122.9 s sweep time and 3 scans. For the Ti centre $[TiO_4/M^+]^0$ the settings used were 350 ± 5 mT scanned magnetic field, modulation amplification 0.5 mT, modulation frequency 100 kHz, 30 ms conversion time and 61.4 s sweep time and 5-8 scans of the spectra. The larger modulation amplitude had to be used for the Ti centre due to the weak signal intensity. The microwave power was always 10 mW. Due to the angular dependency of the ESR signal, a mean signal intensity was calculated by rotating the sample tube 3 times.

The intensity of the Al centre was taken from the first (g = 2.0185) to the last peak (g = 1.9928), as recommended by Toyoda et al. (2000). For the Ti centre, the intensity was taken from the peak at g_3 = 1.913 to the baseline. This includes both Ti-Li and Ti-H centres as we measured the signal with 0.5 mT modulation amplitude and individual intensity measurements of both Ti centres was not possible. An example of the natural ESR composite spectrum of sample NP18-01 with the ESR intensities marked which were used can be found in Fig. 2.

An in-house device, consisting of a heating component which allows temperatures between 100 °C and 600 °C for preheating and annealing, and a Varian VF-50J X-ray tube (50 kV, 1 mA, 50 W) with a tungsten target, was used for all laboratory irradiations and thermal treatments (Oppermann and Tsukamoto, 2015). For this setting, the calibrated dose is 0.3 Gy/s (Tsukamoto et al., 2021).

2.5 Performance tests

Preheat plateau test

Prior to all the equivalent dose measurements, a preheat plateau test (PPT) was carried out to ensure only thermally stable parts of the signal are used for the measurements. A heating step is used prior to natural signal measurements and after each artificial irradiation for both the single aliquot additive dose (SAAD) and single aliquot regenerative dose (SAR) protocols, we used in this study. The SAAD protocol was also used to run the PPT. We used sample SG18-03, which is supposed to be young due to the very weak ESR Ti signal. Preheat temperatures were set to 160, 180, 200 and 220 °C and heating was for 4 minutes. In addition, an aliquot

without thermal treatment was used, referred to as "room temperature". In total three dose steps were added on top the natural signal, reaching from 100 Gy over 500 Gy to 1700 Gy to construct a dose response curve (DRC).

Dose recovery test

In luminescence dating, the dose recovery test is a standard quality test to ensure the accuracy of the SAR protocol (Murray and Wintle, 2003). Tsukamoto et al. (2017) adapted this test for ESR by running a single aliquot regenerative and added dose (SARA) protocol with three dose points. Because of the thermal treatments included in the SAR procedure, the sensitivity of the ESR centres per unit dose may be modified.

In this study, we used a modified version of the test suggested by Tsukamoto et al. (2017), by using one dose point, as we already did in a previous study (Richter and Tsukamoto, 2022). The dose recovery test was performed on three aliquots of sample NP18-09. We added 1053 Gy on top of the natural signal considering this to be the new “natural” signal. The measurements were performed using the SAR protocol and a dose response curve was built with dose steps of 500 Gy, 1198 Gy and 3198 Gy to estimate the D_e. The difference between the D_e values obtained from the natural and natural+1053Gy aliquots was then divided by the added dose (1053 Gy) to calculate the dose recovery ratio.

Additionally, another approach was taken to check for sensitivity changes due to the annealing step in the SAR protocol. This procedure is based on Toyoda et al. (2009) and was later adapted by Fang and Grün (2020). A regenerative-additive plot for the sample NP18-09 was constructed. Two sets of samples consisting of three aliquots each were used. The regenerative dose steps were 90, 700 and 2500 Gy whereas the additive dose steps were 100, 300, 400, 900, 1200 and 2400 Gy.

2.6 Equivalent dose measurements

For a set of samples (NP18 and ZS18), we ran both single aliquot additive dose (SAAD) and SAR measurements to estimate the D_e. The main advantage of SAR over SAAD is that the D_e is interpolated and not extrapolated. Thus, a higher degree of certainty in the determination of the D_e is achieved, as it is not critically depending on the used fitting function (Tsukamoto et al., 2015). For both protocols, the D_e values were calculated by fitting the DRC with a single saturating exponential (SSE) function using Origin 2017 software without any data weighting.

We did not perform a bleaching test to estimate the unbleachable signal component of the Al centre, as we subtract the residual age derived from young samples obtained from the same sedimentary sequence (see section 2.7). Therefore, all apparent Al ages and D_e values given are including the unbleachable signal component.

In case of the SAAD protocol we used a preheat step before the natural measurement and after each artificial irradiation step according to the PPT (200 °C, 4 minutes). For the first aliquot of samples NP18-01 to -05 we did 5 dose steps ranging from 100 to 5000 Gy, whereas for NP18-06 to -09 we used 4 dose steps from 100 to 3800 Gy. Each of the second and third aliquot were irradiated to 4 steps ranging from 300 to 5000 Gy. The same 4 dose steps were used for all aliquots of the ZS18 samples.

We used the ESR SAR protocol after Tsukamoto et al. (2015). This includes a preheating step (200 °C, 4 minutes) before measuring the natural signal. Afterwards the natural signal is depleted by annealing (420 °C, 4 minutes) and the remaining residual signal, arising from peroxy radicals (overlapping the Al centre), is subtracted. Except for the ZS17 samples, when only one aliquot was used, we took three aliquots for each SAR measurement. For NP18, we used 3 dose steps, in various combinations reaching from 90-280 Gy for the first step to 2500-2700 Gy for the last step. In case of ZS18, we did 3 dose steps (400, 1200 and 4000 Gy). The ZS17-01 and -03 sample were irradiated to 250, 1000 and 3000 Gy whereas for the other samples we used 150, 900 and 2900 Gy steps.

2.7 Residual subtraction

Chapot et al. (in this issue) provided the single grain OSL ages for 8 samples from NP and ZS sites. We used the uppermost samples from each of the locations where we have OSL ages to calculate the residual ESR age that would have been measured at the time of deposition. In this study, we calculated residual ages instead of residual doses, because different grain sizes were used for the OSL and ESR measurements. From the uppermost 5 samples, we subtracted the corresponding OSL age from the apparent ESR age to calculate a mean ESR residual age. As mentioned in 2.6, the umbleachable Al centre was not determined by a bleaching experiment, but the contribution of this signal component is removed by subtracting the residual Al age (Timar-Gabor et al., 2020; Richter and Tsukamoto, 2022).

2.8 Grain size analysis

Grain size analysis was performed for samples NP18 and ZS18 at LIAG using a Beckman Coulter LS 13320 laser diffractometer. A quality test was carried out to determine the appropriate amount of material for the measurement. Subsequently, grain size measurements were carried out with a determined grain size interval of 0.4-2000 microns. Generally, the laser obscuration was in the range of 7–10%.

3. Results

3.1 Dose rate

Both, the on-site and laboratory gamma measurements revealed very low doses ranging between 0.21 Gy/ka and 0.37 Gy/ka and 0.20 to 0.35 Gy/ka, respectively. No on-site gamma measurements are available for ZS samples. In addition, total dose rates were very low for all of the samples ranging from 0.47 to 0.90 Gy/ka. All parameters for the dose rate calculation can be found in Table 1. Dose rates are shown in Table 2.

3.2 Performance of the protocols

The Ti centre equivalent doses were ~40 Gy for all temperatures with an error of about the same size. As depicted in Fig. 3, the D_e values from the Al centre was also consistent at all temperature within uncertainty, but the value tends to slightly decrease towards higher preheat temperature and stabilise at 200 and 220 °C. The preheat temperature was set to 200 °C for all measurements. The dose recovery ratio of the Al signal slightly overestimates, reflected in the ratio of 1.24 ± 0.10 whereas the Ti signal shows a ratio close to unity, 0.94 ± 0.04.

Fig. 4A shows the regenerative DRC for the Ti centre with the intensities of the additive dosed samples projected onto the DRC marked as dashed lines. Then the added dose values were plotted against the apparent dose values (plotted in Fig. 4B). The slope is 0.94 ± 0.01, which is in excellent agreement with the test result described above and from this it can be concluded that there is no significant sensitivity change by annealing for the Ti centre when using the SAR protocol.

We tried the same approach for the Al centre but were unable to project more than 4 SAAD intensities onto the regenerative DRC as these signal intensities are much smaller than the SAAD intensities. The slope when plotting apparent dose values against added dose values is >3.

3.3 Equivalent dose

The SAAD measurements revealed the D_e for the Al centre (including the unbleachable signal component) to be in the range from 453 to 1707 Gy for the NP18 site, whereas the D_e for the Ti centre ranges from 204 to 1183 Gy. In the case of the three ZS18 samples, the SAAD D_e values for the Al centre (including the unbleachable signal component) are in the range of 1898 to 2190 Gy and for the Ti centre from 654 to 817 Gy. In detail, the D_e values calculated from the SAAD protocol can be found in supplementary Table A1.

For the NP18 samples, the SAR D_e values are in the range of 390 to 2084 Gy in the case of the Al centre (including the unbleachable signal component) and from 127 to 670 Gy for the Ti centre. The ZS17 and ZS18 samples' Al centre D_e range from 379 to 952 Gy (including the unbleachable signal component). The corresponding Ti centre values go from 172 to 700 Gy. An overview of the D_e values calculated from the SAR protocol can be found in Table 3.

The SAAD D_e are usually much larger than the SAR D_e we calculated: For the NP18 samples 11 to 60 % except for the lowermost sample (NP18-01), where SAAD D_e appears to be 18 % smaller. In addition, the Ti centre D_e generated by the SAAD protocol are 44 to 96 % larger compared to SAR. In case of the ZS18 samples, the SAAD Al D_e are at least doubled and go up to 154 %., whereas the Ti D_e exceeds by 11 to 20 %.

3.4 Residual age subtraction

All ESR ages are significantly older than the OSL ages for the same set of samples. The ESR Al and Ti signals were not completely bleached before burial, and the mean ESR residual age calculated using the SAR protocol is 695 ± 23 ka for the Al centre (including the unbleachable signal component) and 209 ± 13 ka for the Ti centre. As can be seen in Fig. 5 for the samples of the NP site, we plotted the OSL ages, apparent and subtracted ESR ages against the depth below palaeo-surface. Below sample NP18-05 the OSL signal saturates. We used the mean ESR residual age and subtracted it from all apparent ESR ages for the samples NP18-05 to NP18-01. NP 18-05 was used to test whether this subtraction method is robust; the OSL age of this sample (121 ± 5 ka) and the residual subtracted Ti age (134 ± 29 ka) agreed within 1-σ error, confirming the validity of the residual subtraction. The residual subtracted Al age of this sample is also consistent with the OSL age, 170 ± 70 ka, although the uncertainty is larger. The residual subtracted ESR Ti ages of the underlying samples increase to 355 ± 58 ka, 590 ± 86

and 788 ± 89 ka before an age inversion occurs to 534 ± 73 ka for the bottom sample. For the Al centre, the residual subtracted age keeps increasing with depth, but all ages tended to overestimate the Ti centre.

We did the same approach for the ZS site where Chapot et al. (this issue) reported three OSL ages. From this, we calculated a mean ESR residual age of 742 ± 118 ka for the Al centre and 268 ± 39 ka for the Ti centre using the 3 uppermost samples. Again, the sample which yielded the oldest OSL age (161 ± 44 ka; ZS17-06) was used to test the validity of the residual subtraction method. The residual subtracted Ti and Al ages are 237 ± 52 ka and 396 ± 142 ka, respectively, which are consistent with the OSL age within 2 sigma uncertainty. Although the sampling sites are distributed over a wider area, the age trend roughly follows the estimated depth (see Fig. 6).

The ages calculated using the SAAD protocol are higher and show larger standard errors than the SAR ages. Nevertheless, the OSL ages and residual subtracted ESR ages calculated using the SAAD protocol for NP site are consistent within 1-σ uncertainty for the Ti centre and 2-σ uncertainty for the Al centre. The mean SAAD ESR residual ages are 898 ± 97 ka and 409 ± 31 ka for the Al centre and Ti centre, respectively. The SAAD ESR results are plotted in Fig. 7.

A comparison of the subtracted SAAD and SAR Al and Ti ages, and OSL ages plotted against the depth below the palaeo surface for the NP18 site (Fig. A1) show good agreement for sample NP18-05 between the OSL age and all but the subtracted Al age determined by the SAAD protocol. For the samples below, the ages from the different signals and protocols used follow a similar trend and agree within 1-σ uncertainty before disagreeing below NP18-02.

The residual subtracted ESR Ti ages obtained from the SAR protocol and OSL ages in a combination with the profile photos of the NP18 samples can be found in the supplementary (Fig. A2) as well as of the ZS18 samples in Fig. A3. The results using the SAAD protocol are listed in supplementary Table A1. A comparison of the subtracted SAAD and SAR Al and Ti ages, and OSL ages plotted against the depth below the paleo surface for NP18 site can be found in Fig. A3.

3.5 Grain size measurements

The measurements revealed a bimodal grain size distribution for all the investigated samples. In case of the nine NP18 samples, there is a first peak at ~150 microns and a second peak at ~520 microns with a slight tendency to coarsen towards the top of the sand scarp. The three samples of ZS18 have a peak at 150 microns and in the range of 470 to 520 microns, whereas the lowermost sample ZS18-03 shows a slightly larger fine peak and a weaker and finer coarse peak. The grain size distributions are plotted in Fig. 8.

4. Discussion and Conclusion

The grain size measurements revealed a bimodal pattern for all of the analysed samples. Moreover, there is a slight tendency in coarsening towards the top of the gully deposits. This is probably due to input from proximal and distal sediment sources. The overall similarity of the grain size distribution for the samples from the same site indicates that the sedimentary processes were similar through time, and justify the use of the youngest samples for the residual subtraction.

The dose recovery ratio of 0.94 ± 0.04 obtained using the Ti centre suggests that the SAR protocol is working, and this is also confirmed by the sensitivity test using the additive-regenerative plot (Figure 4B). For the Al signal, the dose recovery ratio is ~20% above unity (DR ratio of 1.24 ± 0.10 for NP site), which causes overestimated Al ages. The good recovery behaviour of the Ti centre agrees with previous studies (Tsukamoto et al., 2017, Richter and Tsukamoto, 2022). This indicates the robustness of the ESR SAR protocol applied to the Ti centre.

From the comparison of OSL and ESR ages for the uppermost part of the sand scarp, we found that the ESR signals had a large residual before burial. This follows the study from Richter and Tsukamoto (2022) who also found significant differences in OSL and ESR ages for the same set of fluvial sediment samples. Therefore, if a representative modern analogue sample is available, residual subtraction is highly recommended.

Due to the interpolation used to obtain the D_e, the SAR protocol is preferable to the additive method. Moreover, the dose recovery ratios show that the SAR protocol works satisfyingly for the Ti centre and the standard errors of the ages are lower.

We used a combined approach of quartz OSL and ESR dating to construct a chronology of the sand scarp. These residual ages were subtracted from the apparent ages for the lower part of the section, which led to a smooth transition from OSL ages to ESR ages over the course of

the sequence for the NP site, spanning from 788 ± 89 ka to 13.2 ± 0.7 ka using both ESR (Ti centre) and OSL. The validity of the residual subtraction method was confirmed by the consistent OSL and ESR ages after subtraction for both NP and ZS sites. The combination of OSL and ESR methods is a powerful tool to date Pleistocene sediments.

Within the NP18 sequence, we were able to locate the end of the Early Stone Age (NP18-03) 590 ± 86 ka which gives a maximum age for the beginning of the transition to the Middle Stone Age in this part of south-central Africa (Barham et al., 2015).

Acknowledgements

This work was supported by the Arts and Humanities Research Council of Great Britain (AH/N008804/1). We thank Petra Posimowski and Sabine Mogwitz for ESR sample preparation and gamma spectrometry measurements. We thank Sonja Riemenschneider for grain size analysis measurements.

References

Barham, L., Tooth, S., Duller, G.A.T., Plater, A.J., Turner, S., 2015. Excavations at Site C North, Kalambo Falls, Zambia: New Insights into the Mode 2/3 Transition in South-Central Africa. Journal of African Archaeology 13 (2), 187–214.

Behrensmeyer, A.K., Potts, R., Deino, A., 2018. The Oltulelei Formation of the southern Kenyan Rift Valley: A chronicle of rapid landscape transformation over the last 500 k.y. GSA Bulletin 130 (9-10), 1474–1492.

Brennan, B.J., 2003. Beta doses to spherical grains. Radiat. Meas. 37, 299–303.

Burrough, S.L., Thomas, D.S.G., Barham, L.S., 2019. Implications of a new chronology for the interpretation of the Middle and Later Stone Age of the upper Zambezi Valley. Journal of Archaeological Science: Reports 23, 376–389.

Chapot, M., Duller, G.A.T., Barham, L.S., this issue. Challenges of single grain quartz OSL dating sediment samples from a low dose-rate environment near Victoria Falls in Zambia. Quaternary Geochronology.

406 Coe, D., Barham, L., Gardiner, J., Crompton, R., 2022. A biomechanical investigation of the
407 efficiency hypothesis of hafted tool technology. Journal of The Royal Society Interface 19
408 (188), 20210660.

409 Deino, A.L., McBrearty, S., 2002. 40Ar/39Ar dating of the Kapthurin Formation, Baringo,
410 Kenya. J. Hum. Evol. 42 (1–2), 185–210.

411 Douze, K., Delagnes, A., Rots, V., Gravina, A. B., 2018. Reply to Sahle and Braun's reply to
412 'The pattern of emergence of a Middle Stone Age tradition at Gademotta and Kulkuletti
413 (Ethiopia) through convergent tool and point technologies' [J. Hum. Evol. 91 (2016) 93–121],
414 Journal of Human Evolution, Volume 125: 207-214, ISSN 0047-2484,
415 https://doi.org/10.1016/j.jhevol.2018.04.015.

416 Duller, G.A.T., Tooth, S., Barham, L., Tsukamoto, S., 2015. New archaeological investigations
417 at Kalambo Falls, Zambia: Luminescence chronology and site formation. J. Hum. Evol. 85,
418 111–125.

419 Fang, F., Grün, R., 2020. ESR thermochronometry of Al and Ti centres in quartz: A case study
420 of the Fergusons Hill-1 borehole from the Otway Basin, Australia. Radiat. Meas. 139.

421 Garzanti, E., Pastore, G., Stone, A., Vainer, S., Vermeesch, P., Resentini, A., 2022. Provenance
422 of Kalahari Sand: Paleoweathering and recycling in a linked fluvial-aeolian system. Earth-
423 Science Reviews 224.

424 Guérin, G., Mercier, N., Nathan, R., Adamiec, G., Lefrais, Y., 2012. On the use of the infinite
425 matrix assumption and associated concepts: A critical review. Radiat. Meas. 47, 778–785.

426 Jones, D. L., Duncan, R. A., Briden, J. C., Randall, D. E., MacNiocaill, C., 2001. Age of the
427 Batoka basalts, northern Zimbabwe, and the duration of Karoo Large Igneous Province
428 magmatism. Geochem. Geophys. Geosyst. 2 (2), 2000GC000110.

429 Liritzis, I., Stamoulis, K., Papachristodoulou, C., Ioannides, K., 2013. A re-evaluation of
430 radiation dose-rate conversion factors. Mediterr. Archaeol. Archaeom. 13, 1–15.

431 Murray, A.S., Wintle, A.G., 2003. The single aliquot regenerative dose protocol: potential for
432 improvements in reliability. Radiat. Meas. 37, 377–381.

433 Oppermann, F., Tsukamoto, S., 2015. A portable system of X-ray irradiation and heating for
434 electron spin resonance (ESR) dating. Anc. TL 33, 11–15.

435 Porat, N., Chazan, M., Grün, R., Aubert, M., Eisenmann, V., Horwitz, L.K., 2010. New
436 radiometric ages for the Fauresmith industry from Kathu Pan, southern Africa: Implications for
437 the Earlier to Middle Stone Age transition. J. Archaeol. Sci. 37 (2), 269–283.

438 Prescott, J.R., Hutton, J.T., 1994. Cosmic ray contributions to dose rates for luminescence and
439 ESR dating: large depths and long-term time variations. Radiat. Meas. 23, 497–500.

440 Readhead, M.L., 2002. Absorbed dose fraction for 87Rb beta particles. Anc. TL 20, 25–29.

441 Richter, D., Grün, R., Joannes-Boyau, R., Steele, T.E., Amani, F., Rué, M., Fernandes, P.,
442 Raynal, J.P, Geraads, D., Ben-Ncer, A., Hublin, J-J., McPherron, S.P., 2017.The age of the
443 hominin fossils from Jebel Irhoud, Morocco, and the origins of the Middle Stone Age. Nature
444 546 (7657), 293–296.

445 Richter, M., Tsukamoto, S., 2022. Investigation of quartz ESR residual signals in the last glacial
446 and early Holocene fluvial deposits from the Lower Rhine. Geochronology 4, 55–63.

447 Rots, V., & Plisson, H., 2014. Projectiles and the abuse of the use-wear method in search for
448 impact. Journal of Archaeological Science 48, 154–165.

449 Sahle, Y., Hutchings, W.K., Braun, D.R., Sealy, J.C., Morgan, L.E., Negash, A., Atnafu, B.,
450 2013. Earliest Stone-Tipped Projectiles from the Ethiopian Rift Date to >279,000 Years Ago.
451 PLOS ONE 8 (11), 1–9.

452 Thomas, D.S.G., Burrough, S.L., 2016. Luminescence-based dune chronologies in southern
453 Africa: Analysis and interpretation of dune database records across the subcontinent.
454 Quaternary International 410, 30–45.

455 Timar-Gabor, A., Chruscinska, A., Benzid, K., Fitzsimmons, K., Begy, R., Bailey, M., 2020.
456 Bleaching studies on Al hole ([AlO4/h]0) electron spin resonance (ESR) signal in sedimentary
457 quartz. Radiat. Meas. 130, 106–221.

458 Tissoux, H., Toyoda, S., Falguères, C., Voinchet, P., Takada, M., Bahain, J.-J., Despriée, J.,
459 2008. ESR Dating of Sedimentary Quartz from Two Pleistocene Deposits Using Al and Ti-
460 Centers. Geochronometria 30, 23–31.

461 Toyoda, S., Miura, H., Tissoux, H., 2009. Signal regeneration in ESR dating of tephra with
462 quartz. Radiat. Meas. 44, 483–487.

463 Toyoda, S., Voinchet, P., Falguères, C., Dolo, J. M., Laurent, M., 2000. Bleaching of ESR
464 signals by the sunlight: a laboratory experiment for establishing the ESR dating of sediments,
465 Applied Radiation and Isotopes 52, 1357–1362.

466 Tryon, C.A., McBrearty, S., Texier, P.-J., 2006. Levallois Lithic Technology from the
467 Kapthurin Formation, Kenya: Acheulian Origin and Middle Stone Age Diversity. African
468 Archaeological Review 22 (4), 199–229.

469 Tsukamoto, S., Oppermann, F., Autzen, M., Richter, M., Bailey, M., Ankjærgaard, C., & Jain,
470 M., 2021. Response of the Ti and Al electron spin resonance signals in quartz to X-ray
471 irradiation. Radiat. Meas. 149, 106676.

472 Tsukamoto, S., Long, H., Richter, M., Li, Y., King, G. E., He, Z., Yang, L., Zhang, J., Lambert,
473 R., 2018. Quartz natural and laboratory ESR dose response curves: A first attempt from Chinese
474 loess, Radiat. Meas. 120, 137–142.

475 Tsukamoto, S., Porat, N., Ankjærgaard, C., 2017. Dose recovery and residual dose of quartz
476 ESR signals using modern sediments: Implications for single aliquot ESR dating, Radiat. Meas
477 106, 472–476.

478 Tsukamoto, S., Toyoda, S., Tani, A., Oppermann, F., 2015. Single aliquot regenerative dose
479 method for ESR dating using X-ray irradiation and preheat. Radiat. Meas. 81, 9–15.

480 Voinchet, P., Toyoda, S., Falguères, C., Hernandez, M., Tissoux, H., Moreno, D., Bahain, J.-J.,
481 2015. Evaluation of ESR residual dose in quartz modern samples, an investigation on
482 environmental dependence, Quaternary Geochronology 30, 506–512.

483 Wilkins, J., Schoville, B.J., Brown, K.S., Chazan, M., 2012. Evidence for early hafted hunting
484 technology. Science 338 (6109), 942–946.

Table 1: Parameters for dose rate calculation and HPGe gamma spec results. Water content is 5 ± 2 %. The depth is below palaeo surface with a 50 % error assumed.

Sample ID	Altitude (m)	Depth (m)	Uranium (ppm)	Thorium (ppm)	Potassium (%)
NP18-09	977	1 ± 0.5	0.81 ± 0.06	2.87 ± 0.18	0.05 ± 0.01
NP18-08	977	1 ± 0.5	0.69 ± 0.03	2.73 ± 0.15	0.03 ± 0.01
NP18-07	975	2.4 ± 1.2	0.81 ± 0.04	3.15 ± 0.17	0.04 ± 0.01
NP18-06	971	3.5 ± 1.8	0.87 ± 0.05	3.33 ± 0.18	0.04 ± 0.01
NP18-05	966	5.4 ± 2.7	0.87 ± 0.04	3.45 ± 0.18	0.04 ± 0.01
NP18-04	963	6 ± 3	0.84 ± 0.05	3.32 ± 0.19	0.04 ± 0.01
NP18-03	960	7.2 ± 3.6	0.88 ± 0.05	3.59 ± 0.19	0.05 ± 0.01
NP18-02	957	8.5 ± 4.3	0.87 ± 0.05	3.50 ± 0.21	0.05 ± 0.01
NP18-01	946	16.5 ± 8.3	0.73 ± 0.06	3.44 ± 0.21	0.50 ± 0.04
ZS17-04	977	3.5 ± 2	0.75 ± 0.02	3.45 ± 0.04	0.05 ± 0.01
ZS17-05	976	4.5 ± 2.5	0.75 ± 0.02	3.21 ± 0.04	0.04 ± 0.01
ZS17-06	974	6 ± 2.5	0.79 ± 0.02	3.32 ± 0.04	0.04 ± 0.01
ZS17-07	973	7.5 ± 3	0.79 ± 0.02	3.58 ± 0.03	0.04 ± 0.01
ZS18-01	964	7.5 ± 3.8	0.81 ± 0.04	3.47 ± 0.18	0.04 ± 0.01
ZS17-09	971	9 ± 3	0.76 ± 0.02	3.93 ± 0.04	0.02 ± 0.01
ZS17-08	971	9.5 ± 3	0.64 ± 0.02	3.19 ± 0.03	0.04 ± 0.01
ZS18-02	960	9.5 ± 4.8	0.81 ± 0.04	3.45 ± 0.18	0.06 ± 0.01
ZS18-03	960	9.5 ± 4.8	0.75 ± 0.04	3.29 ± 0.17	0.06 ± 0.01
ZS17-01	960	11.5 ± 3.5	0.85 ± 0.02	4.06 ± 0.04	0.07 ± 0.01
ZS17-03	956	11.5 ± 3.5	0.72 ± 0.02	3.61 ± 0.04	0.07 ± 0.01

Table 2: Composition of the total dose rate. The mean gamma dose rate is composed of the field and laboratory dose.

Sample ID	Cosmic dose rate (Gy/ka)	Beta dose rate (Gy/ka)	Field gamma dose rate (Gy/ka)	Lab gamma dose rate (Gy/ka)	Mean gamma dose rate (Gy/ka)	Total dose rate (Gy/ka)
NP18-09	0.20 ± 0.03	0.19 ± 0.01	0.21 ± 0.01	0.23 ± 0.01	0.22 ± 0.02	0.61 ± 0.04
NP18-08	0.20 ± 0.03	0.16 ± 0.01	0.21 ± 0.01	0.20 ± 0.01	0.21 ± 0.02	0.56 ± 0.03
NP18-07	0.16 ± 0.03	0.19 ± 0.01	0.24 ± 0.01	0.24 ± 0.01	0.24 ± 0.02	0.59 ± 0.04
NP18-06	0.14 ± 0.04	0.20 ± 0.01	0.24 ± 0.01	0.25 ± 0.01	0.25 ± 0.02	0.58 ± 0.04
NP18-05	0.11 ± 0.04	0.20 ± 0.01	0.26 ± 0.01	0.26 ± 0.01	0.26 ± 0.02	0.57 ± 0.04
NP18-04	0.10 ± 0.04	0.19 ± 0.01	0.27 ± 0.01	0.25 ± 0.01	0.26 ± 0.02	0.56 ± 0.05
NP18-03	0.09 ± 0.04	0.21 ± 0.01	0.27 ± 0.01	0.27 ± 0.02	0.27 ± 0.02	0.57 ± 0.05
NP18-02	0.08 ± 0.04	0.21 ± 0.01	0.28 ± 0.01	0.26 ± 0.02	0.27 ± 0.02	0.56 ± 0.05
NP18-01	0.04 ± 0.03	0.50 ± 0.03	0.37 ± 0.03	0.35 ± 0.02	0.36 ± 0.03	0.90 ± 0.05
ZS17-04	0.14 ± 0.04	0.20 ± 0.01	n.a.	0.25 ± 0.01	n.a.	0.59 ± 0.04
ZS17-05	0.13 ± 0.04	0.18 ± 0.01	n.a.	0.23 ± 0.01	n.a.	0.55 ± 0.04
ZS17-06	0.11 ± 0.03	0.19 ± 0.01	n.a.	0.24 ± 0.01	n.a.	0.54 ± 0.04
ZS17-07	0.09 ± 0.03	0.20 ± 0.01	n.a.	0.26 ± 0.01	n.a.	0.54 ± 0.04
ZS18-01	0.09 ± 0.04	0.19 ± 0.01	n.a.	0.25 ± 0.01	n.a.	0.53 ± 0.04
ZS17-09	0.08 ± 0.03	0.19 ± 0.01	n.a.	0.26 ± 0.01	n.a.	0.53 ± 0.03
ZS17-08	0.07 ± 0.02	0.17 ± 0.01	n.a.	0.22 ± 0.01	n.a.	0.47 ± 0.03
ZS18-02	0.07 ± 0.04	0.21 ± 0.01	n.a.	0.26 ± 0.01	n.a.	0.54 ± 0.04
ZS18-03	0.07 ± 0.04	0.20 ± 0.01	n.a.	0.24 ± 0.01	n.a.	0.51 ± 0.04
ZS17-01	0.06 ± 0.02	0.23 ± 0.01	n.a.	0.29 ± 0.01	n.a.	0.59 ± 0.03
ZS17-03	0.06 ± 0.02	0.21 ± 0.01	n.a.	0.26 ± 0.01	n.a.	0.53 ± 0.03

Table 3: Equivalent doses derived from the SAR protocol, apparent and residual subtracted ages. The mean ESR residual ages are 695± 23 ka and 209 ± 13 ka for the Al centre and Ti centre, respectively for NP site, and 742 ± 118 ka and 268 ± 39 ka for ZS site.

Sample ID	ESR D_e (SAR)		Apparent ESR age		Qz OSL ages	ESR Residual age		Residual subtracted ESR age	
	Al centre (Gy)	Ti centre (Gy)	Al centre (ka)	Ti centre (ka)	(ka)	Al centre (ka)	Ti centre (ka)	Al centre (ka)	Ti centre (ka)
NP18-09	425 ± 17	145 ± 1	701 ± 47	240 ± 13	13.2 ± 0.7	688 ± 47	227 ± 13	n.a.	n.a.
NP18-08	425 ± 19	142 ± 5	756 ± 52	252 ± 17	14.1 ± 0.7	742 ± 52	238 ± 17	n.a.	n.a.
NP18-07	390 ± 9	127 ± 3	661 ± 42	215 ± 14	40.9 ± 1.9	620 ± 42	175 ± 14	n.a.	n.a.
NP18-06	435 ± 35	144 ± 9	744 ± 78	246 ± 23	63.7 ± 3.5	681 ± 78	183 ± 23	n.a.	n.a.
NP18-05	495 ± 11	196 ± 4	865 ± 66	343 ± 26	120.7 ± 4.9	745 ± 67	222 ± 27	170 ± 70	134 ± 29
NP18-04	683 ± 21	314 ± 20	1227 ± 103	564 ± 57	n.a.	n.a.	n.a.	532 ± 106	355 ± 58
NP18-03	778 ± 21	455 ± 34	1365 ± 110	798 ± 85	n.a.	n.a.	n.a.	670 ± 112	590 ± 86
NP18-02	886 ± 81	557 ± 24	1586 ± 190	997 ± 88	n.a.	n.a.	n.a.	890 ± 192	788 ± 89
NP18-01	2084 ± 523	670 ± 54	2310 ± 594	742 ± 72	n.a.	n.a.	n.a.	1615 ± 594	534 ± 73
ZS17-04	416 ± 7	175 ± 2	708 ± 53	298 ± 22	60 ± 2.9	648 ± 53	238 ± 22	n.a.	n.a.
ZS17-05	379 ± 5	172 ± 15	694 ± 58	316 ± 37	93.5 ± 4.2	601 ± 58	222 ± 37	n.a.	n.a.
ZS17-06	616 ± 5	274 ± 5	1138 ± 78	506 ± 35	160.5 ± 43.5	977 ± 89	345 ± 56	396 ± 142	237 ± 52
ZS17-07	772 ± 10	451 ± 10	1424 ± 95	831 ± 57	n.a.	n.a.	n.a.	682 ± 152	563 ±69
ZS18-01	862 ± 27	550 ± 22	1612 ± 135	1029 ± 90	n.a.	n.a.	n.a.	870 ± 179	761 ± 98
ZS17-09	680 ± 18	394 ± 6	1292 ± 82	747 ± 45	n.a.	n.a.	n.a.	550 ± 144	479 ± 59
ZS17-08	907 ± 27	583 ± 15	1947 ± 130	1251 ± 82	n.a.	n.a.	n.a.	1205 ± 176	982 ±90
ZS18-02	952 ± 30	680 ± 21	1778 ± 145	1269 ± 103	n.a.	n.a.	n.a.	1036 ± 187	1001 ± 110
ZS18-03	942 ± 5	700 ± 19	1842 ± 145	1368 ± 113	n.a.	n.a.	n.a.	1100 ± 187	1100 ± 120
ZS17-01	776 ± 60	649 ± 18	1324 ± 120	1108 ± 61	n.a.	n.a.	n.a.	582 ± 169	840 ± 72
ZS17-03	733 ± 6	528 ± 3	1391 ± 71	1001 ± 51	n.a.	n.a.	n.a.	649 ± 138	733 ± 64

Fig. 1: A) Satellite image of the southern part of the African continent with the location of Victoria Falls marked. B) Satellite image of the Victoria Falls with the sampling locations marked: In the north, the white oval marks the sampling locations located in the Mosi oa Tunya National Park, close to the airport premises. Songwe sampling location is marked in the south. C) Close-up satellite image of the National park with the sampling locations roughly marked. All images from google earth.

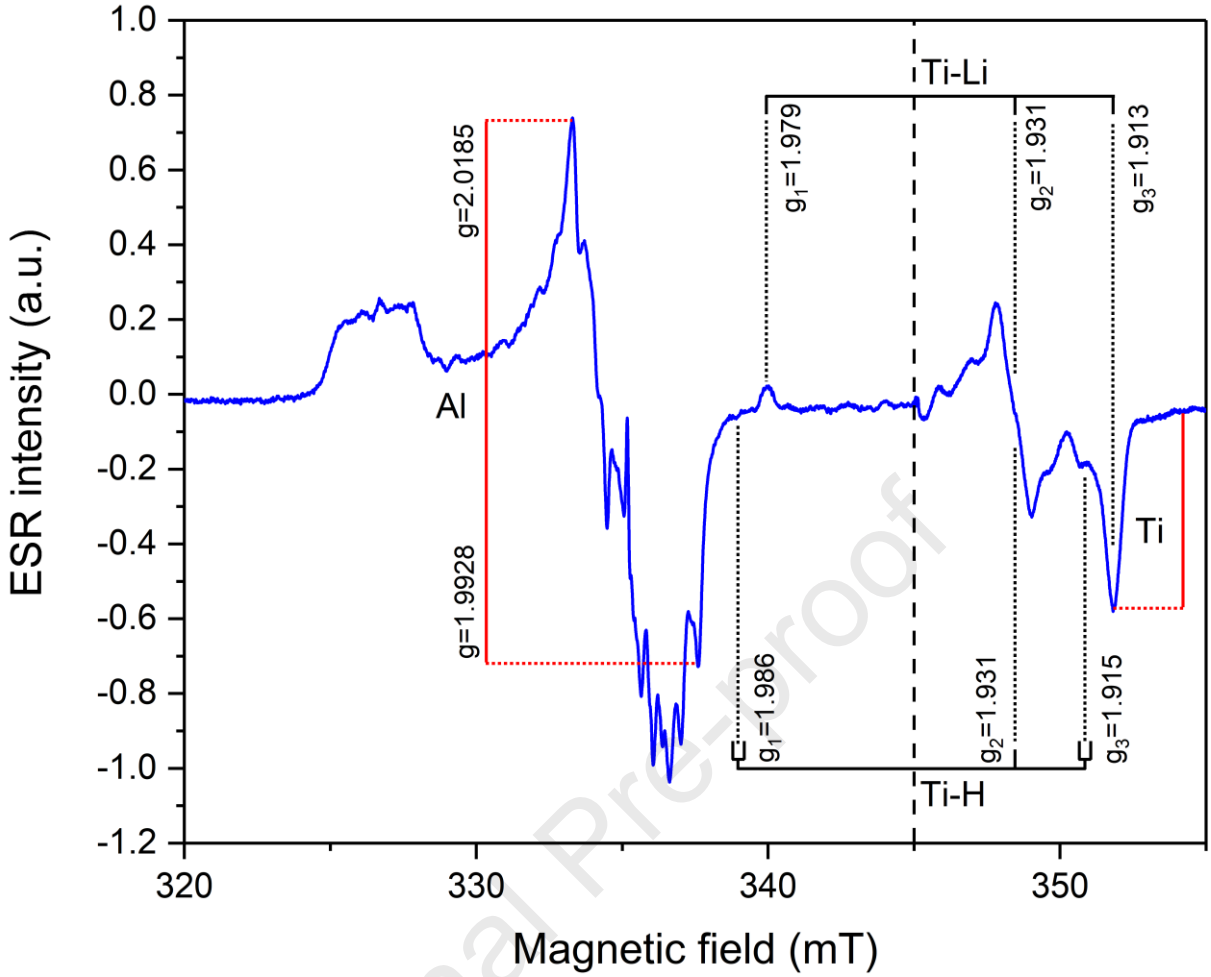

Fig. 2: Natural ESR spectrum of sample NP18-01. The Al and Ti signal intensities used in this study are indicated in red colour. Please note that this is not a continuous spectrum, as indicated by the dashed line. The Al and the Ti centre were recorded with different measurement parameters: notably left from the dashed lines with 0.1 mT modulation amplification and 0.5 mT on the right side, respectively. Detailed information is given in the text.

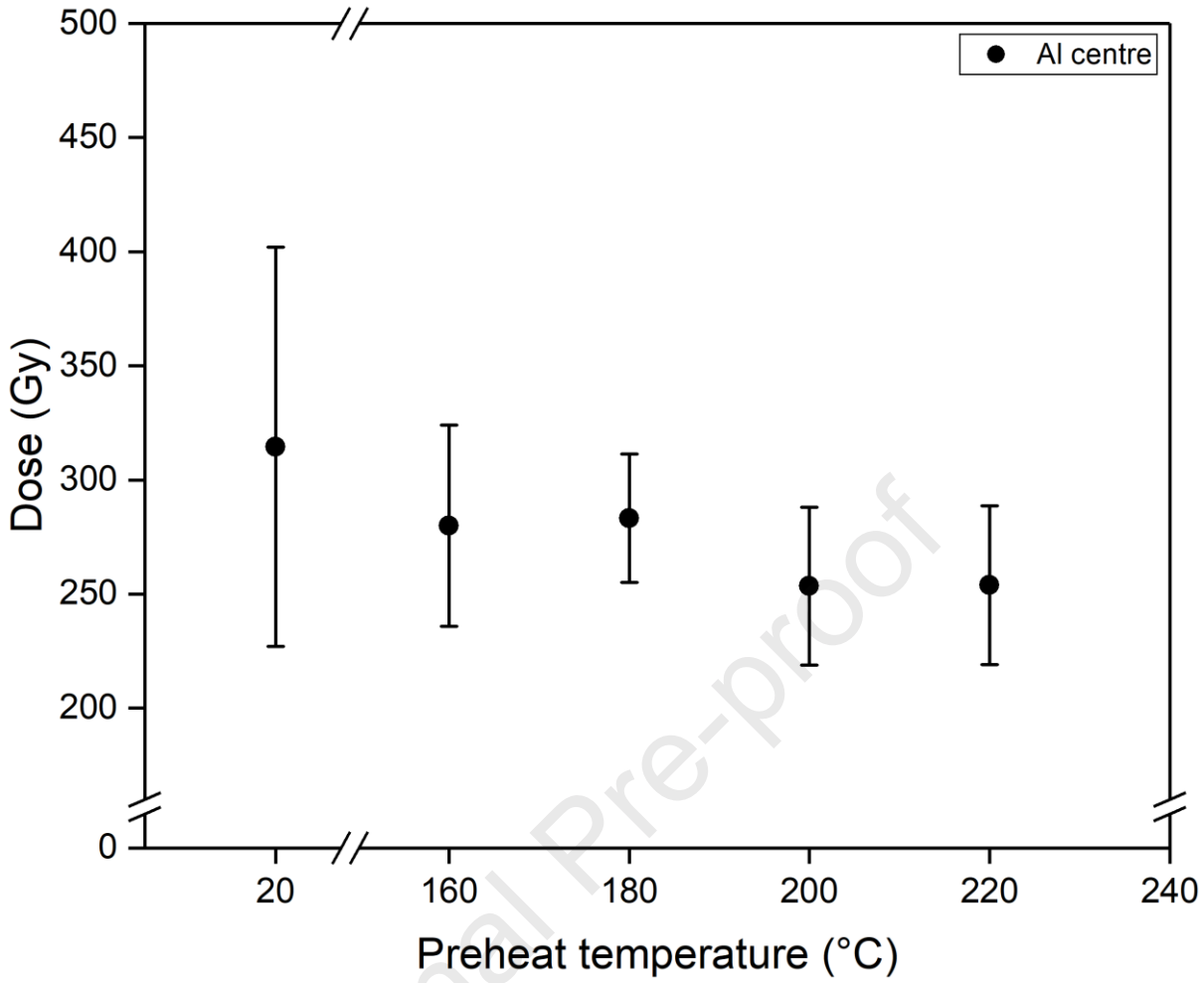

Fig. 3: Preheat plateau test of sample SG18-03.

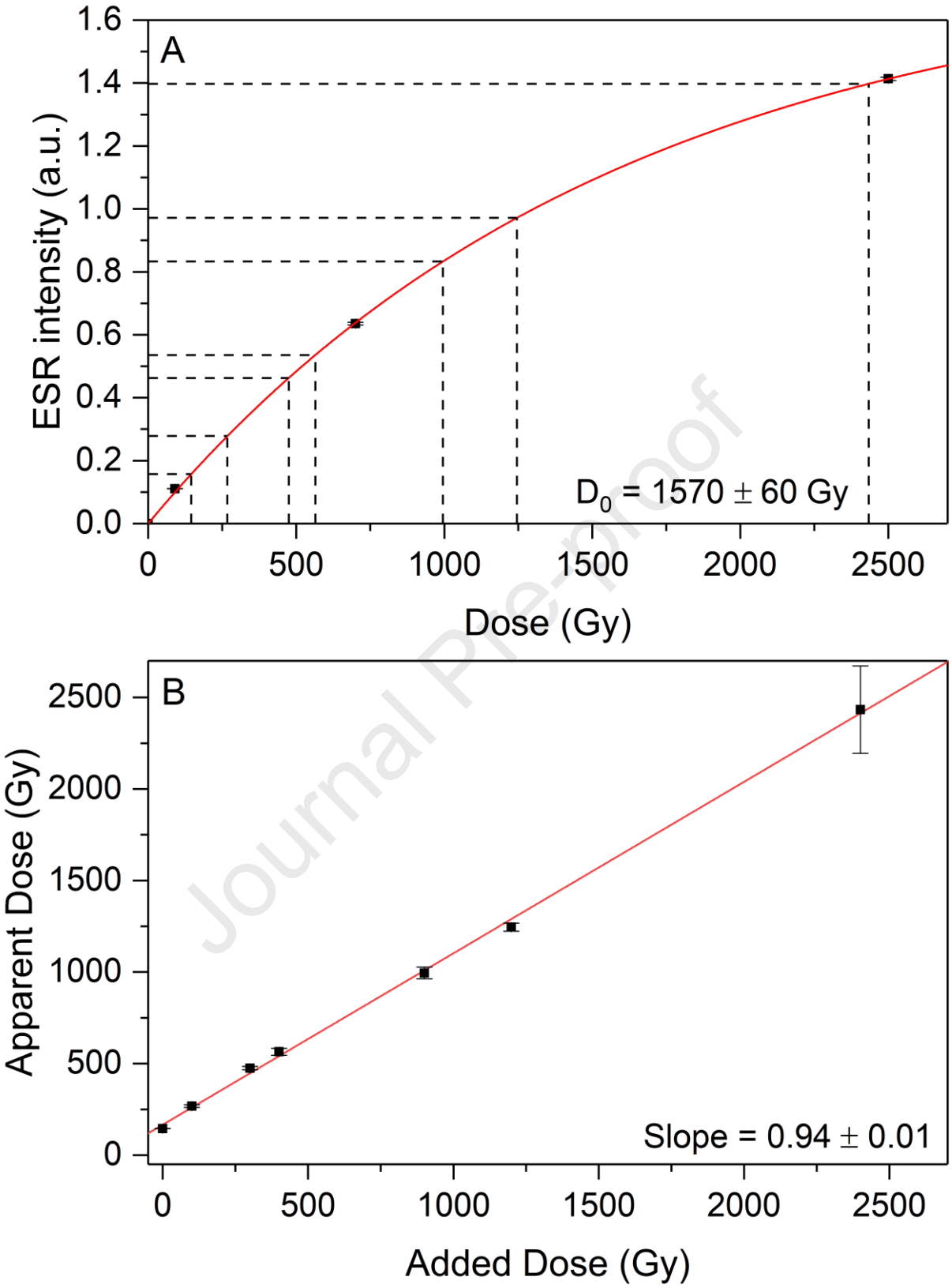

Fig. 4: A) Regenerative dose response curve of the Ti centre fitted by SSE function. Dashed lines mark the additive intensities and doses, respectively. B) The regenerative-additive plot for the Ti centre.

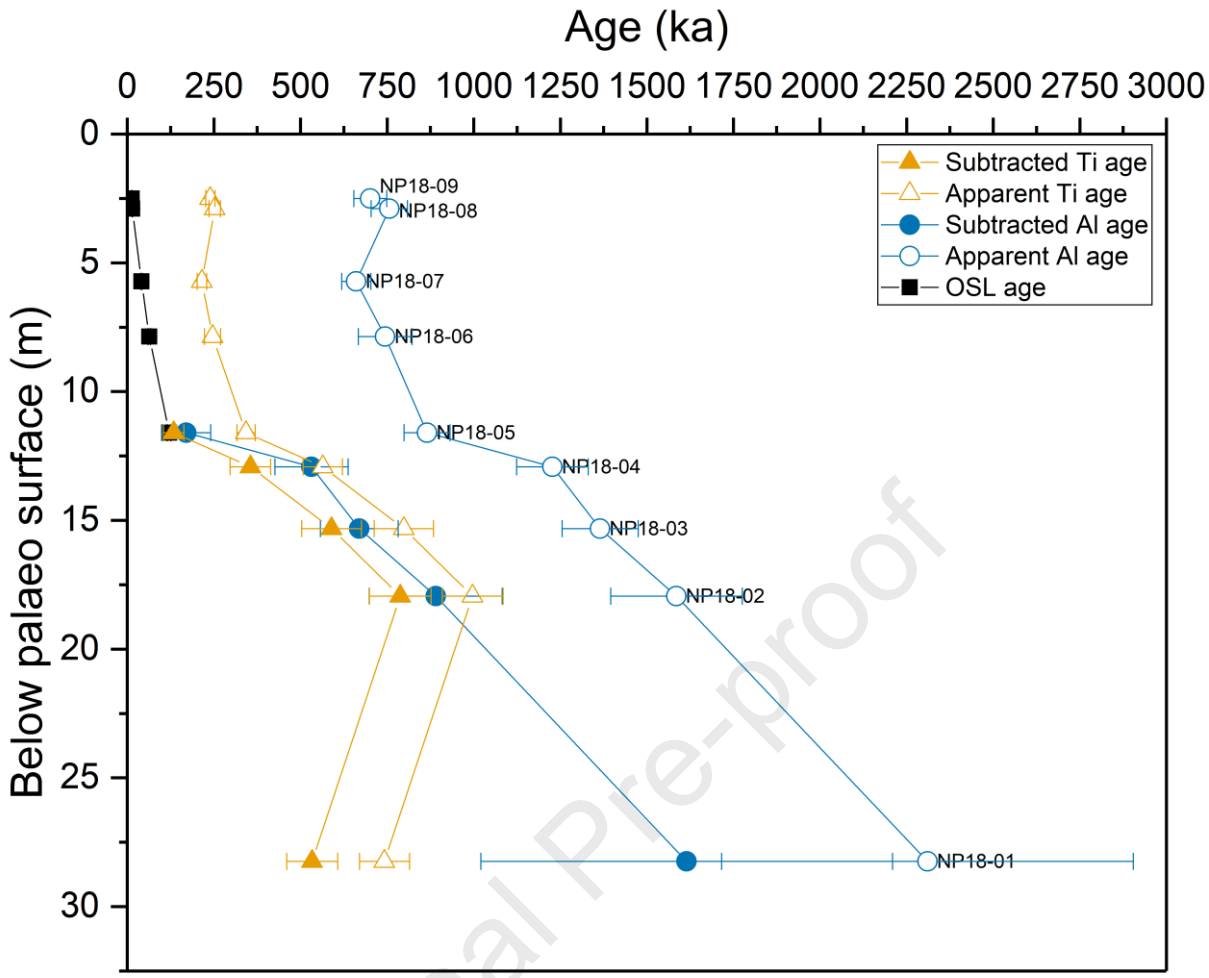

Fig. 5: The OSL ages, apparent SAR ESR Al and Ti ages, and the subtracted ESR Al and Ti ages for NP18 samples plotted against the depth below palaeo surface.

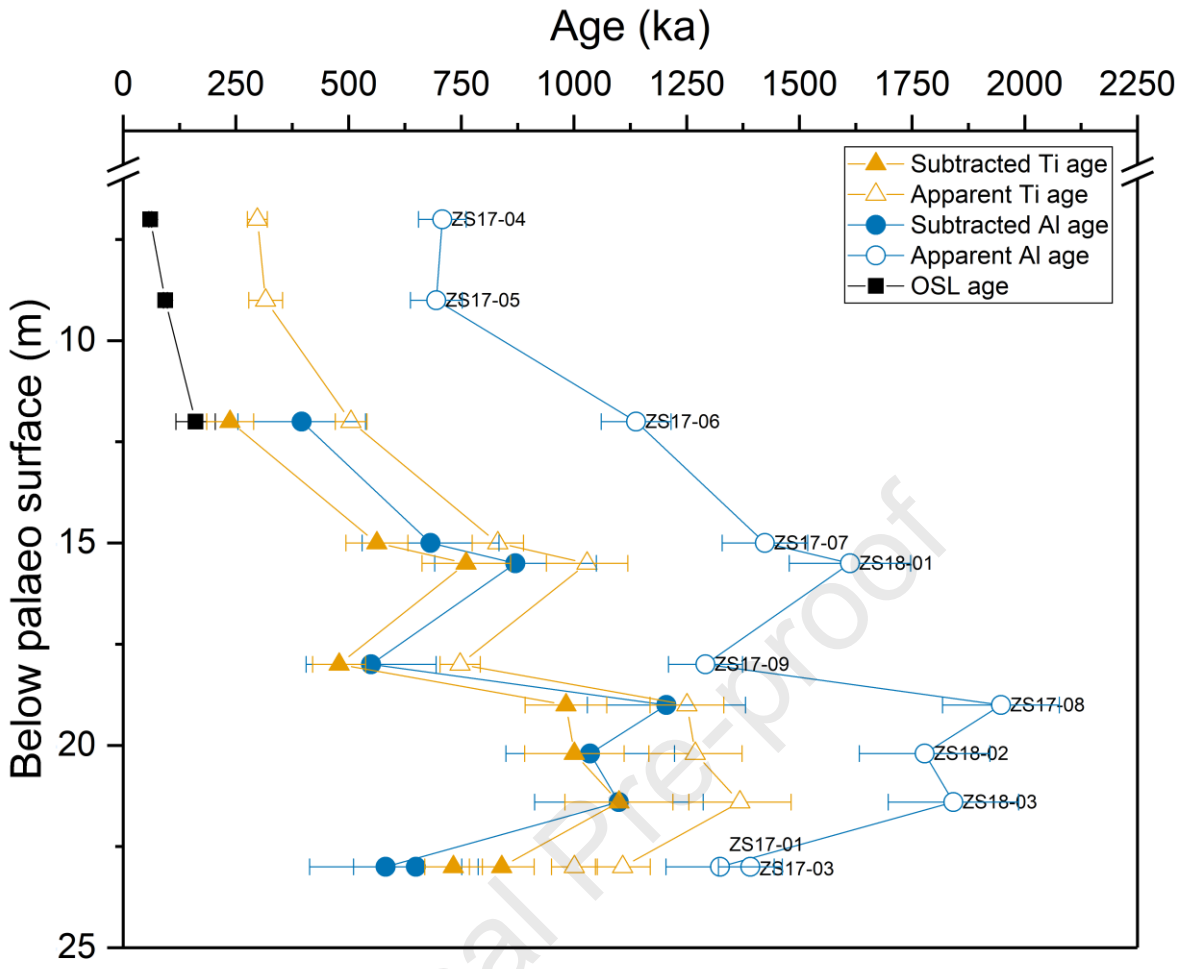

Fig. 6: The OSL ages, apparent SAR ESR Al and Ti ages, and the subtracted ESR Al and Ti ages for ZS17/18 samples plotted against the depth below palaeo surface.

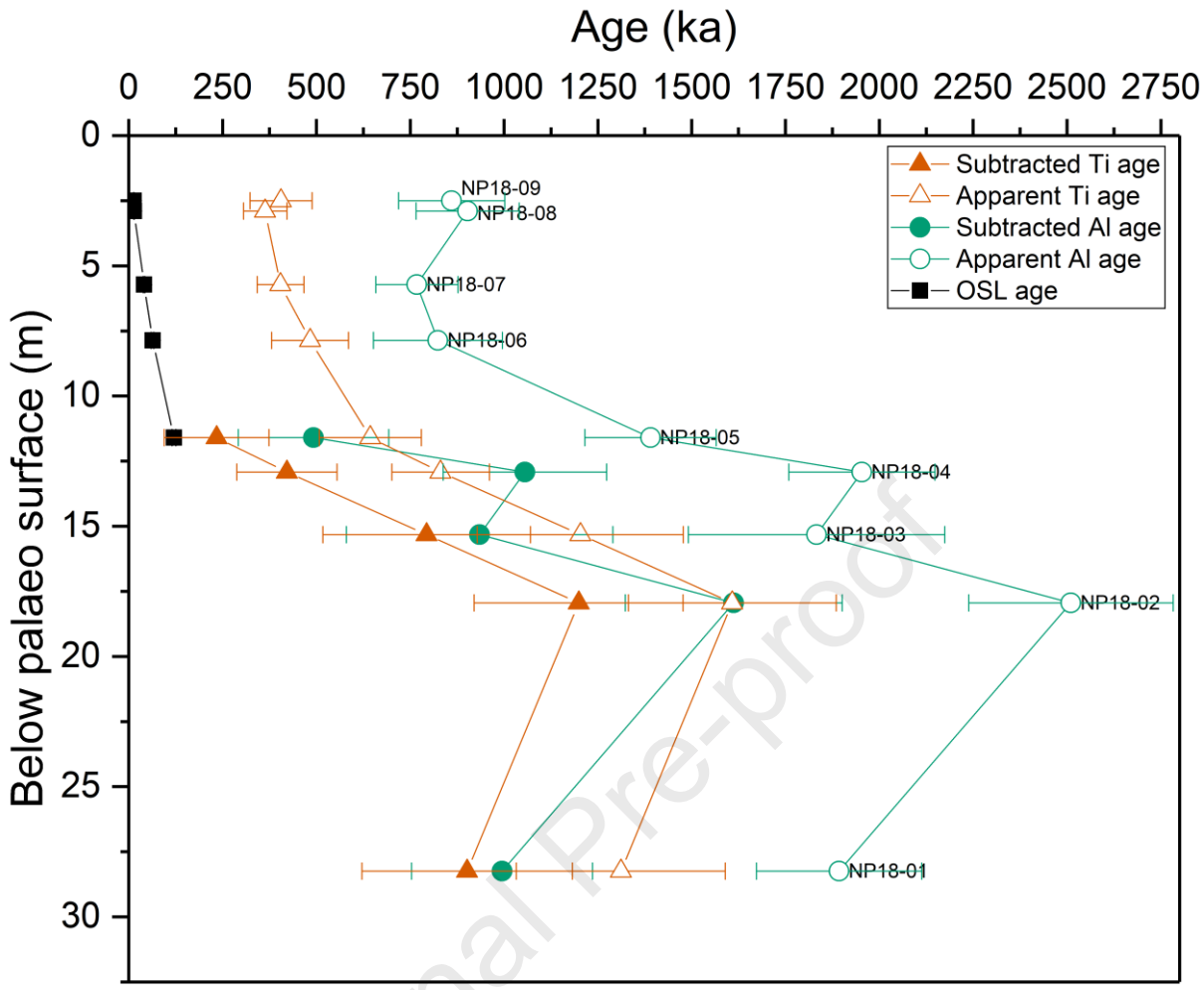

Fig. 7: The OSL ages, apparent SAAD ESR Al and Ti ages, and the subtracted ESR Al and Ti ages for NP18 samples plotted against the depth below palaeo surface.

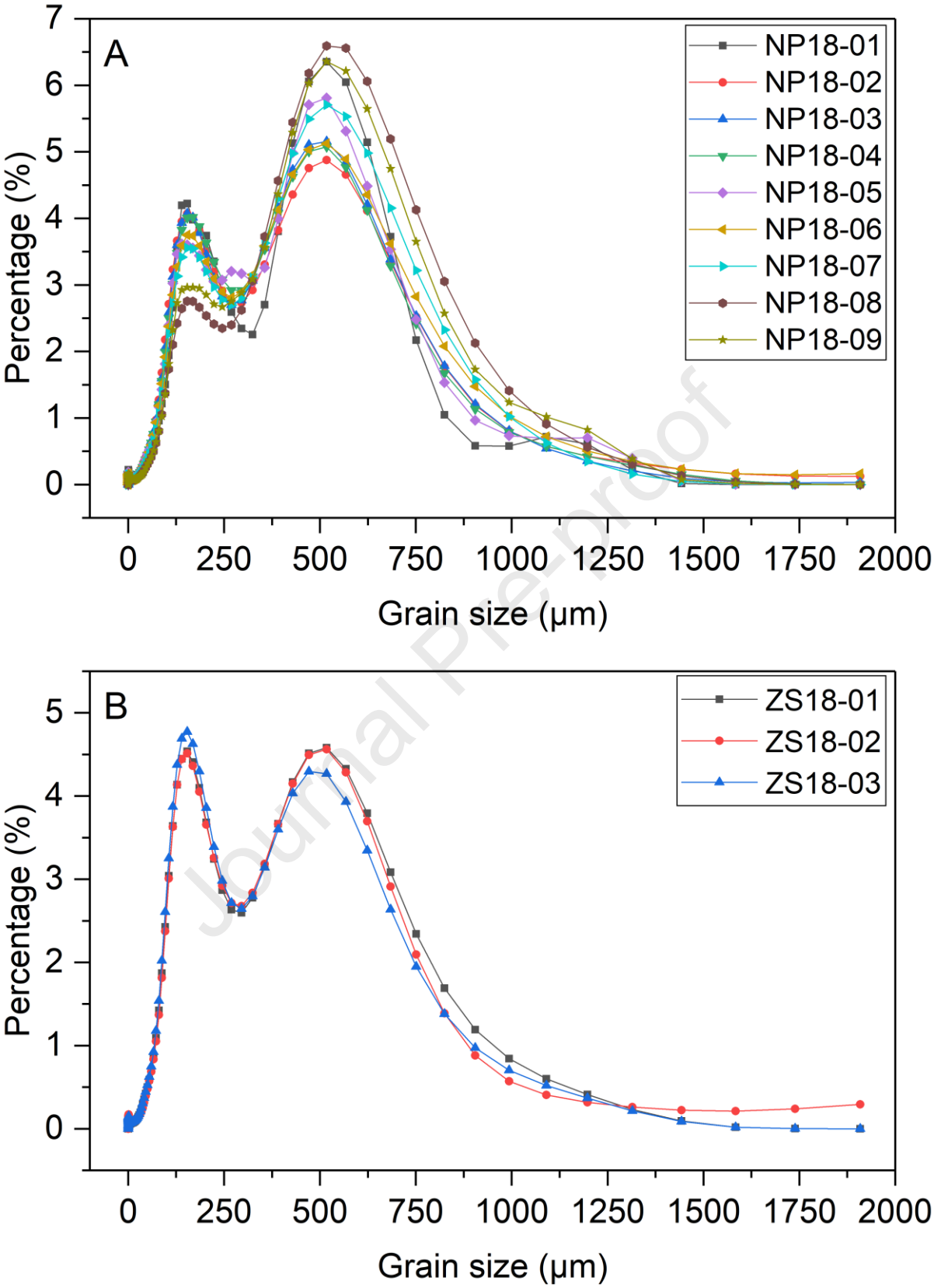

Fig. 8: Grain size distribution plots for A) NP18 and B) ZS18 samples showing a bimodal distribution.

Declaration of interests

☒ The authors declare that they have no known competing financial interests or personal relationships that could have appeared to influence the work reported in this paper.

☐The authors declare the following financial interests/personal relationships which may be considered as potential competing interests: